scientific reports

Check for updates

OPEN

# Synergistic Fe-Mn-Cu ternary alloys enhance bifunctional activity and stability for alkaline water splitting

Amir Kazempour, Saleh Moradi-Alavian, Habib Ashassi-Sorkhabi & Elnaz Asghari✉

**Developing cost-effective, high-performance electrocatalysts for water splitting remains a critical challenge for advancing renewable energy technologies. Herein, we present a novel ternary alloy catalyst, 20Fe-80Mn-20Cu, designed and optimized for hydrogen evolution (HER) and oxygen evolution reactions (OER). The catalyst, synthesized via electrodeposition, demonstrates exceptional bifunctional activity and stability, outperforming binary (20Fe-80Mn) and benchmark electrodes, such as Pt and DSA. Linear sweep voltammetry (LSV) revealed that 20Fe-80Mn-20Cu requires a remarkably low overpotential (without iR drop correction) of 172 mV for HER and 147 mV for OER to achieve a current density of 10 mA $cm^{-2}$, significantly surpassing the performance of binary alloys and bare substrates. Tafel slope analysis further confirmed the catalytic efficiency, with values of 53 mV $dec^{-1}$ for HER and 56 mV $dec^{-1}$ for OER. Electrochemical impedance spectroscopy (EIS) revealed low charge transfer resistance, highlighting the alloy's excellent electron transport properties. Raman and XRD investigations revealed the catalyst's unique structural and compositional features, including extra crystallographic reflections indicating increased surface activity. Stability tests conducted at ± 250 mA $cm^{-2}$ over 4 days demonstrated excellent durability, with only 7% (HER) and 5% (OER) performance drops. Post-stability characterizations, including XRD and EDX, revealed Mn and Fe redistribution and Cu enrichment on the surface, as well as the formation of stable copper oxides under OER conditions. These findings establish 20Fe-80Mn-20Cu as a promising candidate for scalable water splitting, offering an energy-saving potential of up to 5.5 V per $cm^2$ of the electrode surface. This study increases our understanding of alloy-based catalysts and demonstrates a feasible approach for efficient and sustainable hydrogen production.**

**Keywords** Fe-Mn-Cu catalyst, Electrodeposition, Water splitting, Energy conversion materials

Research on effective methods of utilizing renewable energy sources has increased due to global demand for clean and sustainable energy[1–4]. Among various alternatives, hydrogen stands out due to its high energy density and zero emissions during use[5–8]. However, there are significant obstacles to clean hydrogen production, particularly from water splitting[9]. The development of water-splitting technologies still depends on the efficient hydrogen evolution (HER) and oxygen evolution reactions (OER), which call for highly efficient, stable, and reasonably priced catalysts[10–15].

Traditional catalysts, which are frequently based on noble metals such as platinum and iridium, have remarkable HER and OER performance but are expensive and restricted in availability, making them unsuitable for large-scale applications[16–20]. To overcome this issue, researchers are increasingly focusing on earth-abundant transition metals, especially elements like iron (Fe), copper (Cu), and manganese (Mn)[21–24]. These elements not only provide cost savings but also possess synergistic properties that could enhance catalytic efficiency and stability when combined. Fe and Cu, for example, are well-studied in binary alloy systems for electrochemical applications, whereas Mn brings unique electronic configurations that might further improve the material's performance, particularly in terms of OER activity[25–27].

Recent advances in non-noble electrocatalysts have highlighted the potential of transition metal alloys for water splitting, yet achieving bifunctional activity and long-term stability remains challenging. While binary Fe-Mn systems exhibit promising OER activity[28,29] and Fe-Cu alloys show excellent HER performance[30], their single-function nature and susceptibility to degradation limit practical applications.

In this work, we report a novel Fe-Mn-Cu ternary alloy catalyst synthesized via electrodeposition. This approach leverages the catalytic strengths of Fe and Cu, while Mn improves active site density and structural

Electrochemistry Research Laboratory, Department of Physical Chemistry, Faculty of Chemistry, University of Tabriz, Tabriz, Iran. ✉email: elnazasghari@yahoo.com; e.asghari@tabrizu.ac.ir

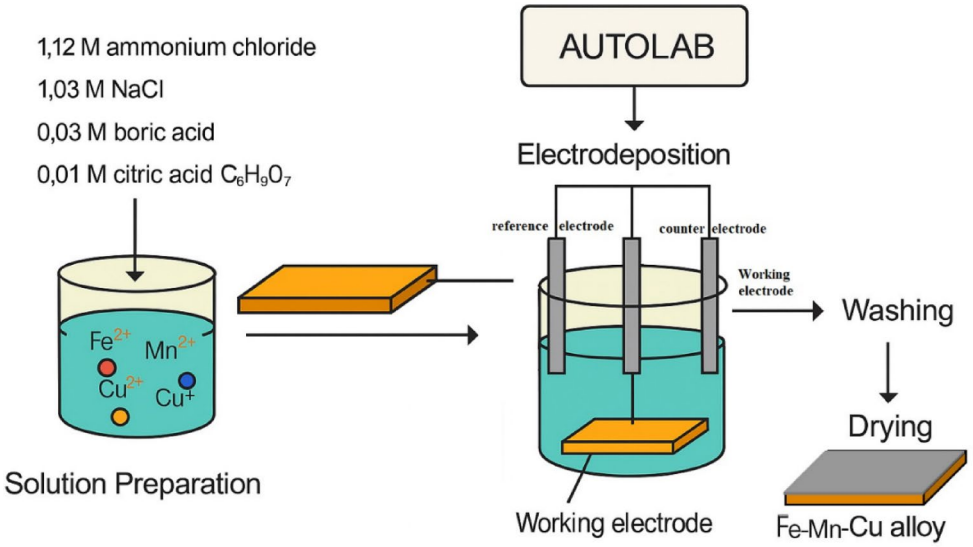


**Fig. 1**. Schematic presentation of electrodeposition steps of alloys.

| Samples | $Fe^{2+}$ (mM) | $Mn^{2+}$ (mM) | $Cu^{2+}$ (mM) |
|---|---|---|---|
| 20Fe-80Mn | 20 | 80 | 0 |
| 40Fe-60Mn | 40 | 60 | 0 |
| 50Fe-50Mn | 50 | 50 | 0 |
| 60Fe-40Mn | 60 | 40 | 0 |
| 80Fe-20Mn | 80 | 20 | 0 |
| 20Fe-80Mn-xCu | 20 | 80 | x = 10, 20,40,80 |

**Table 1**. Different concentrations of coating metals and samples name.

integrity under reaction conditions. The resulting alloy features a uniform morphology and high metal dispersion, minimizing phase separation typically observed in multi-metal systems.

To the best of our knowledge, this is among the first studies to report a Fe-Mn-Cu ternary alloy for overall water splitting, addressing both HER and OER in a single material platform. The simultaneous optimization of cost, bifunctionality, and structural integrity makes this alloy system distinctly innovative in the growing field of non-noble-metal-based electrocatalysts. Furthermore, our study offers a rare combination of synthesis simplicity and multifunctionality, backed by a comprehensive set of electrochemical characterizations. The unique compositional tuning and observed high performance establish this material as a competitive and scalable candidate for green hydrogen production.

## Experimental

### Preparation of catalysts

The Fe-Mn-Cu alloy electrodes were made via electrodeposition at constant potentials on a 1 $cm^2$ steel substrate. The alloy formation was facilitated by the presence of 1.12 M ammonium chloride ($NH_4Cl$), 1.03 M sodium chloride (NaCl), 0.03 M boric acid ($H_3BO_3$), and 0.01 M citric acid ($C_6H_8O_7$) in the deposition bath. The average catalyst loading mass on the 1 $cm^2$ substrate for the best-performing electrode was approximately 25 mg, determined from three independent measurements. Schematic electrodeposition of prepared electrodes is shown in Fig. 1.

As shown in Table 1, different concentrations of $FeSO_4$, $MnSO_4$, and $CuSO_4$ were added to the bath to tailor the elemental composition of the electrodeposited alloy. Controlled deposition of Fe, Mn, and Cu was made possible by conducting electrodeposition for 1200 s at various potentials of -1, -1.5, -2, and – 2.5 V. This range of potentials was chosen in order to assess how the applied potential affected the catalytic performance of the alloy. To provide a clean, consistent surface, the steel substrate was polished, cleaned with deionized water, and dried before deposition. The coated electrodes were carefully cleaned with deionized water after electrodeposition and allowed to air dry before being subjected to electrochemical testing and further characterization.

### Electrochemical measurement

Electrochemical tests were carried out to assess the catalytic efficacy of the Fe-Mn-Cu alloy coating for HER and OER. Linear sweep voltammetry (LSV) was performed in a three-electrode configuration with a potential range

of -2 to +2 V and a scan rate of 1 mV $s^{-1}$, using 1 M KOH solution as the electrolyte. A graphite sheet was used as the counter electrode, a saturated calomel electrode (SCE) as the reference electrode, and a Fe-Mn-Cu-coated steel substrate as the working electrode. The generated LSV curves are shown without the iR drop correction. Electrochemical impedance spectroscopy (EIS) measurements were used to determine the charge transfer resistance during HER and OER. Nyquist plots were taken at potentials of -1.2 V for HER and +2 V for OER over a frequency range of 100 kHz to 10 mHz, with a sinusoidal amplitude of 10 mV. Chronopotentiometric measurements in 1 M KOH solution were used to examine electrode stability in a two-electrode arrangement with a graphite sheet serving as anode or cathode. The coated electrodes were evaluated for 4 days with a steady current of -250 mA for HER and +250 mA for OER. The electrochemical active surface area (ECSA) was determined using the procedure described in our previous work[58].

### Characterization techniques

The morphologies and chemical structures of prepared catalysts were analyzed using the MIRA3 FEG Tescan field emission scanning electron microscope (FESEM) equipped with an EDX and MAP spectroscope, Tensor 27 Bruker Fourier transform infrared (FTIR) spectrometer, and X-ray diffractometer (Philips PW1730) with Cu-Kα radiation (λ = 1.540°A). Furthermore, Raman spectroscopy was carried out with the Andor BT127AL Raman spectrometer, which had a 532 nm laser wavelength. Inductively coupled plasma optical emission spectroscopy (ICP-OES) (Model 5000DV, PG Instruments, UK) was used to assess the concentration of metal ions released during electrochemical stability tests.

## Results and discussion

### Characterization of catalysts

The Raman spectra of the 20Fe-80Mn and 20Fe-80Mn-20Cu alloys (Fig. 2a) show a few important differences that are consistent with the literature on metal alloying and structural modification effects in catalytic materials. Peaks at 206, 265, 366, 447, 578, 640, and 1282 $cm^{-1}$ indicate Fe-O and Mn-O vibrational modes in the binary 20Fe-80Mn alloy. These peaks are largely consistent with the predicted modes for Fe and Mn oxides or mixed oxides, indicating that the binary alloy may include some oxide surface passivation. We see variations in peak locations for the ternary alloy (20Fe-80Mn-20Cu), including at around 213, 277, 381, 589, and 622 $cm^{-1}$[31–36]. Notably, the lack of the 447 $cm^{-1}$ peak indicates that the local bonding environment is altered by the addition of Cu, possibly inhibiting a particular Mn-O vibrational mode. According to published research[37], the addition of Cu may cause the lattice symmetry of Fe-Mn oxide to be broken, changing vibrational modes or suppressing certain Mn-related peaks as a result of lattice strain or Cu-introduced electronic interactions. Shifts in Raman peak locations are frequently related to alloy formation since atomic bonding lengths alter with Cu inclusion. The occurrence of the 1282 $cm^{-1}$ peak in both binary and ternary alloys may suggest a stable vibrational characteristic connected to a specific structural motif or Fe-Mn bonding environment, which remains mainly unaffected by the addition of Cu. Overall, the Raman spectroscopic analysis confirms the successful synthesis and structural modification of the 20Fe-80Mn-20Cu ternary alloy. The characteristic shifts in Fe-O/Mn-O vibrational modes (206–640 $cm^{-1}$) and the disappearance of the 447 $cm^{-1}$ peak upon Cu incorporation demonstrate significant alterations in the local bonding environment, consistent with effective alloy formation. The preservation of the 1282 $cm^{-1}$ feature indicates structural stability of the Fe-Mn matrix, while the observed peak shifts and mode suppression verify Cu-induced lattice distortion and electronic interactions. These spectroscopic signatures collectively validate the formation of a true ternary alloy system with modified structural properties, rather than a simple mixture of constituent metals, confirming the success of the synthesis protocol in creating a homogeneous, chemically integrated material.

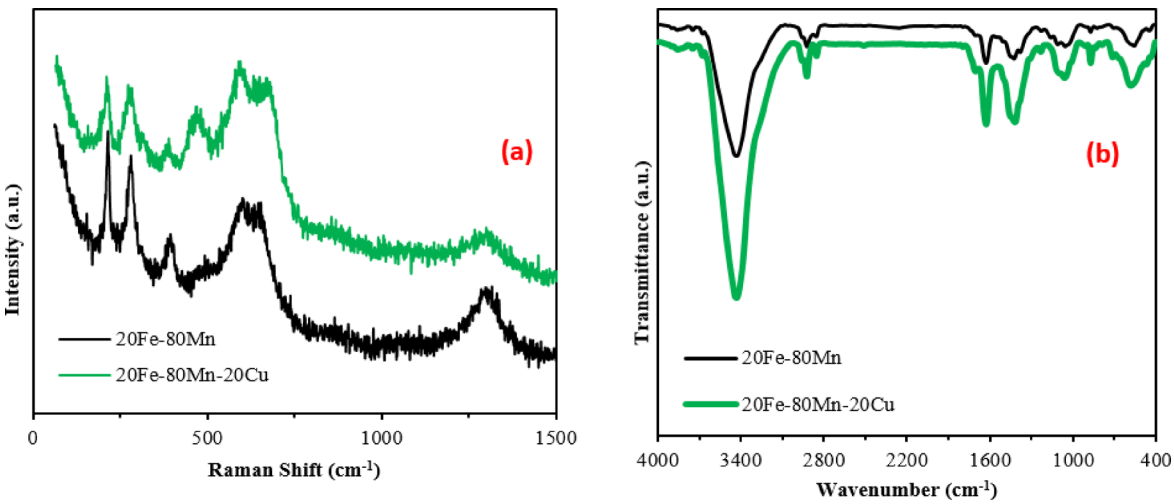


**Fig. 2**. Electrodeposited electrode's characterizations: (**a**) Raman and (**b**) FT-IR spectra.

The IR spectra of 20Fe-80Mn and 20Fe-80Mn-20Cu alloys (Fig. 2b) show similar prominent peaks, indicating a fairly constant structural framework across both compositions; however, small shifts to lower wavenumbers in the ternary alloy reflect Cu inclusion alterations. The relatively wide peak at 3464 $cm^{-1}$, caused by O-H stretching vibrations of surface hydroxyl groups or adsorbed water, indicates a small change in the ternary alloy, presumably due to altered hydrogen bonding or hydration states impacted by Cu. Peaks at 2974 and 2905 $cm^{-1}$, indicating C-H stretching (perhaps from leftover organics), and the band at 1653 $cm^{-1}$, linked with H-O-H bending, show modest redshifts, indicating changed surface interactions. Furthermore, the 1472 $cm^{-1}$ peak, which may relate to surface carbonate species[38], along with bands at 1110, 885, and 617 $cm^{-1}$ (attributed to M-O lattice vibrations), are all marginally shifted in the ternary alloy[39]. These shifts suggest slight changes in the metal-oxide lattice and surface structure. These changes are consistent with literature observations that Cu incorporation can impact the bonding and electrical environment in Fe-Mn systems, implying that the alloy's catalytic surface may display improved interaction dynamics with adsorbed species in the presence of Cu[40]. Overall, the FTIR analysis confirmed the successful synthesis of the 20Fe-80Mn-20Cu ternary alloy while revealing subtle Cu-induced modifications to the material's surface chemistry. The preservation of major vibrational features (3464 $cm^{-1}$ O-H, 1653 $cm^{-1}$ H-O-H, and 617 $cm^{-1}$ M-O modes) confirms structural consistency with the binary alloy, while systematic redshifts in key peaks (C-H, carbonate, and lattice vibrations) demonstrate Cu's electronic influence on the Fe-Mn matrix. These spectroscopic changes - particularly the modified metal-oxygen vibrations and altered surface hydroxyl behavior - provide clear evidence of Cu incorporation into the alloy structure rather than simple physical mixing. The observed shifts in surface-adsorbed species (water, carbonates) and lattice modes collectively verify the formation of a homogeneous ternary system with distinct interfacial properties, suggesting the potential for enhanced catalytic interactions at the alloy-electrolyte interface.

The XRD patterns of both the 20Fe-80Mn and 20Fe-80Mn-20Cu alloys (Fig. 3) show a strong, noticeable peak at 45°, which is normally associated with Fe and Cu phases[41]. The peak located at 65° is related to Fe and two peaks presented at 52° and 74° are attributed to Cu, respectively[42,43]. This peak in the ternary alloy is wider than in the binary alloy, signifying a smaller crystallite size or an increase in lattice strain, which might result from Cu integration into the alloy matrix[44].

Furthermore, the slight shoulder seen on this peak in the ternary alloy implies phase segregation or the creation of a secondary phase, most likely connected to Cu, which is consistent with Cu's known ability to modify crystallographic environments in Fe-based systems[45]. The extra peak detected at 74° in the ternary alloy, which was lacking in the binary, might represent a new phase formation or increased crystallinity of Cu-rich areas, as Cu integration can cause crystallographic changes that appear at higher diffraction angles. Furthermore, while Mn may not produce distinct peaks due to its low crystallinity or tendency toward amorphous states, the literature suggests that Mn incorporation can still influence lattice structure by broadening peaks and subtly altering phase characteristics in the absence of distinct diffraction peaks. This view is consistent with prior observations that Mn may integrate into the alloy in a less crystalline state, possibly improving the alloy's catalytic capabilities by increasing defect sites and lattice strain[46].

The coming sections will cover certain other characterizations of the alloys, such as SEM images and EDX analysis.

## Results from LSV diagrams

Binary Fe-Mn alloys with varying Fe and Mn concentrations were first investigated to optimize the catalyst composition for the highest electrochemical activity. Figure 4a depicts the LSV diagrams for these alloys, specifically 20Fe-80Mn, 40Fe-60Mn, 50Fe-50Mn, 60Fe-40Mn, and 80Fe-20Mn, where the numbers represent the millimolar concentrations of Fe and Mn salts in the electrodeposition bath. The catalysts were produced at a constant potential of -1 V, and their HER and OER activities were evaluated.

The catalytic performance of each Fe-Mn alloy was compared at defined current densities. For HER, the overpotentials (without the iR drop correction) at -100 mA $cm^{-2}$ were recorded as -872 mV for 80Fe-20Mn, -672 mV for 40Fe-60Mn, -633 mV for 50Fe-50Mn, -597 mV for 60Fe-40Mn, and −565 mV for 20Fe-80Mn.

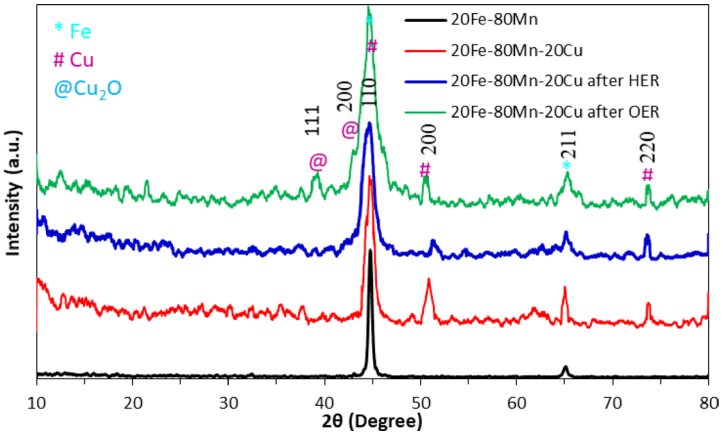


**Fig. 3**. XRD patterns of different electrodeposited coatings.

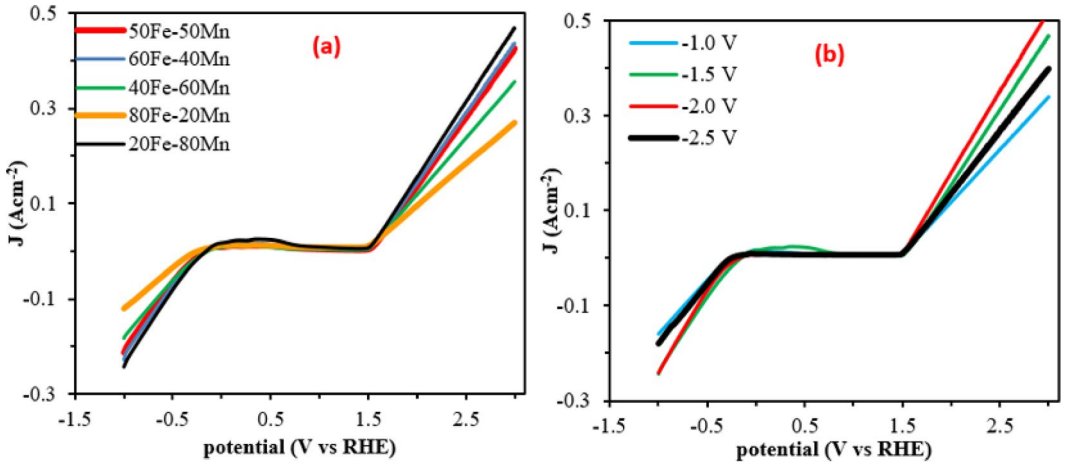


**Fig. 4**. LSV diagrams of electrodeposited electrodes in KOH 1 M: (**a**) Optimization of concentration at −1 V electrodeposition potential and (**b**) 20Fe-80Mn electrode at different electrodeposition potentials.

For OER, at a current density of 100 mA $cm^{-2}$, the overpotentials without the iR drop correction were observed as 797 mV for 80Fe-20Mn, 695 mV for 40Fe-60Mn, 648 mV for 50Fe-50Mn, 628 mV for 60Fe-40Mn, and 600 mV for 20Fe-80Mn. These results demonstrated that the three catalysts 50Fe-50Mn, 60Fe-40Mn, and 20Fe-80Mn had roughly equal HER/OER catalytic performance (and significantly better than 80Fe-20Mn and 40Fe-60Mn), with 20Fe-80Mn having somewhat greater activity. As a result, 20Fe-80Mn was selected as the optimum one at this stage for further investigations. Some interconnected variables may be responsible for the higher catalytic activity of 20Fe-80Mn than the other compositions. First, there could be more active sites as a result of the greater Mn content. Manganese can improve catalytic performance in alloy form, especially when alloyed with transition metals like iron, even though it is frequently less catalytically active when employed alone. By changing the electrical environment of nearby Fe atoms, Mn atoms in the Fe-Mn alloy may produce structural changes that improve surface reactivity. By enhancing the adsorption of intermediates essential for HER and OER, this electrical modulation probably lowers overpotentials and energy barriers. Additionally, the higher Mn concentration in the 20Fe-80Mn alloy could enhance oxygen affinity and make it easier for oxygen-containing intermediates to stabilize during OER. By stabilizing surface-bound oxygen intermediates, manganese is known to aid in OER; this is especially advantageous at higher Mn contents. This may help to explain why 20Fe-80Mn has a lower overpotential for OER than other Fe-Mn alloys with lower Mn contents. The HER pathway is probably also impacted by the alloying effect because Fe and Mn may work together to balance the energy requirements of hydrogen adsorption and desorption. Because 20Fe-80Mn optimizes the adsorption/desorption kinetics, it may provide a favorable binding strength for hydrogen intermediates, thereby facilitating HER. Because effective desorption is limited by higher hydrogen binding energies, the surface of alloys with a higher Fe content (like 80Fe-20Mn) may be less conducive to efficient hydrogen evolution. In the subsequent phase of the study, the influence of electrodeposition potential on the catalytic efficiency of the optimized 20Fe-80Mn alloy was systematically examined; with LSV measurements obtained for catalysts deposited at potentials of -1, -1.5, -2, and − 2.5 V (refer to Fig. 4b). Among the tested catalysts, the specimen deposited at -2 V demonstrated higher performance in both HER and OER, as indicated by the lowest overpotentials recorded.

The SEM images (see Fig. 5) illustrate significant morphological variations in the 20Fe-80Mn alloys deposited at -1 and − 2 V, with the alloy deposited at -1 V exhibiting a pronounced rough surface texture, whereas the one deposited at -2 V presents a markedly smoother surface morphology. The alloy deposited at -2 V exhibited better catalytic activity, which may be explained by the surface composition and morphology, both of which are affected by the deposition potential. A more uniform, dense, and fine-grained deposition might enhance electron transfer and reveal more catalytically active sites[47,48], when electrodeposition potentials are lower, such as -2 V. This smooth, uniform surface likely reduces the barrier to electron flow, thereby lowering the overpotential for both HER and OER.

The rougher morphology produced by deposition at -1 V, however, may be the result of slower nucleation rates and larger particle formations. This can reduce the number of exposed active sites and obstruct effective electron transport. Furthermore, a deposition potential of -2 V would provide a more advantageous alloy composition as, under these circumstances, more Mn might integrate into the Fe matrix, maximizing the electronic structure for catalysis. According to EDX analysis and mapping images for 20Fe-80Mn at the two potentials (see Figs. 6 and 7), the Mn content increased from 12w% at −1 V to 18w% at −2 V. Previous studies[49] suggest that the alloy's catalytic efficiency is enhanced when the Mn and Fe atoms are more uniformly distributed, as this can promote desirable electronic interactions and active site exposure. Therefore, the reaction kinetics for both HER and OER are improved by the smooth morphology and maybe improved Fe-Mn alloying at −2 V, illustrating why this deposition potential is favorable for catalytic activity.

To interpret the effect of Cu addition on the catalytic performance of the Fe-Mn alloy for water splitting, Cu salt was introduced into the deposition bath in varying concentrations (10, 20, 40, and 80 mM) to form a ternary 20Fe-80Mn-xCu alloy at a constant potential of -2 V. Figure 8a presents the LSV diagrams of 20Fe-80Mn-

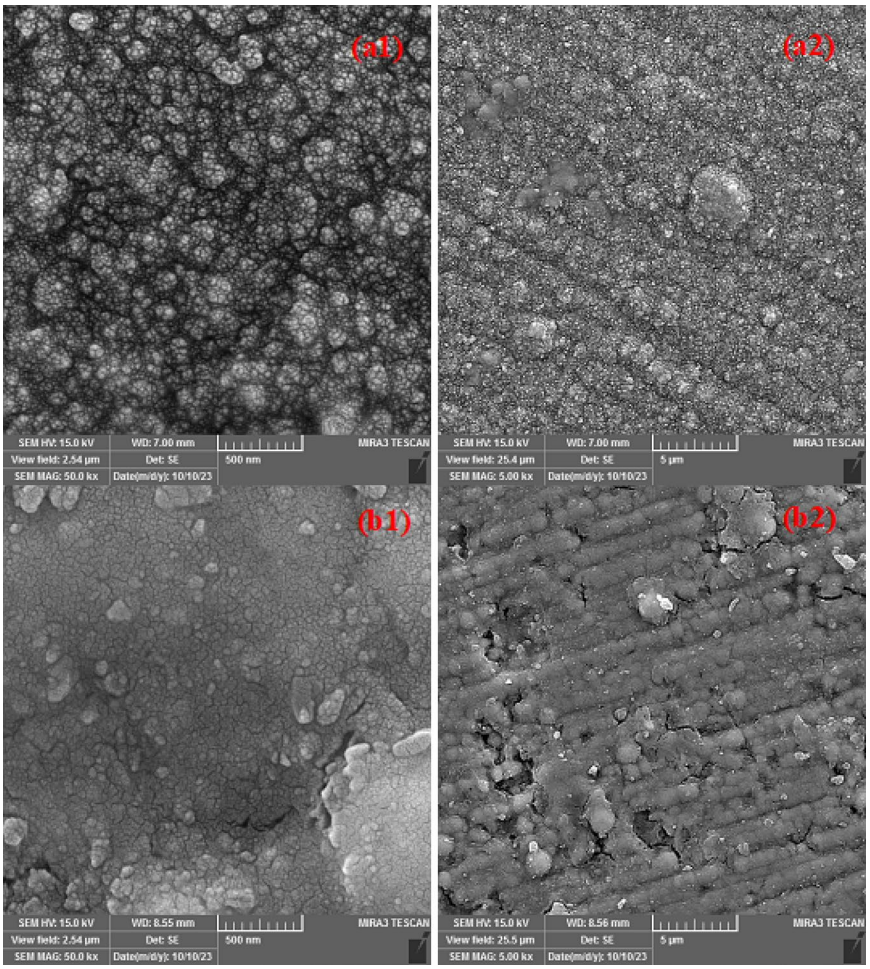


**Fig. 5**. FE-SEM images of electrodeposited 20Fe-80Mn at different potentials: (**a**) electrodeposited at −1 V and (**b**) electrodeposited at −2 V.

xCu catalysts exhibiting varying Cu concentrations, wherein the 20Fe-80Mn-20Cu alloy exhibited the highest catalytic activity for both HER and OER. Based on EDX analysis and corresponding mapping images (Figs. 9 and 10), this optimal alloy composition was found to comprise approximately 8wt% Mn and 43wt% each of Fe and Cu, whereas the SEM images (Fig. 11) revealed a significant shift in surface morphology from the smooth texture of the binary 20Fe-80Mn alloy to a unique granular structure with spherical-like features. The spherical structure of TEM images 20Fe-80Mn-20Cu alloy illustrated in Fig. 12. TEM analysis of the electrodeposited 20Fe-80Mn-20Cu alloy reveals grain sizes ranging from about10 to 100 nm.

Figure 8b presents the 20Fe-80Mn-20Cu alloy polarization curves obtained at different scan rates. Based on the LSV results, the HER region shows negligible changes in the voltammograms with increasing scan rate. In contrast, the OER region exhibits a slight current enhancement, particularly at higher potentials. In the intermediate potential range between the onset of HER and OER, the increase in scan rate leads to a rise in current, attributed to the adsorption/desorption of intermediates and the background current from the electrolyte. Figure 8c demonstrates the electrochemical performance of the synthesized electrode in different electrolytes. The highest current density is observed in the acidic medium compared to other electrolytes, with the HER activity surpassing that of OER under acidic conditions. In contrast, the alkaline environment exhibits the lowest onset potential for the OER.

The enhanced catalytic performance observed in the 20Fe-80Mn-20Cu alloy is probably due to a combination of morphological and compositional variables. Because of its well-known catalytic activity in HER and OER, copper is typically used to improve electrochemical stability and facilitate effective charge transfer. By adding more active sites and maximizing the adsorption energy of reaction intermediates for water splitting, the addition of Cu to the Fe-Mn system probably alters the alloy's electrical environment. According to published research[50,51], Cu can contribute electron density and modify the oxidation states of nearby Fe and Mn atoms to create synergistic electronic effects when alloyed with these metals.

This could result in more efficient stabilization of catalytic intermediates and lower energy barriers for both reactions. Additionally, the morphological change associated with the inclusion of Cu is noteworthy. Cu may predominate the surface morphology, providing its distinctive grain structure and probably increasing surface roughness, as seen by the change from a smooth surface in 20Fe-80Mn to one with spherical grains in 20Fe-

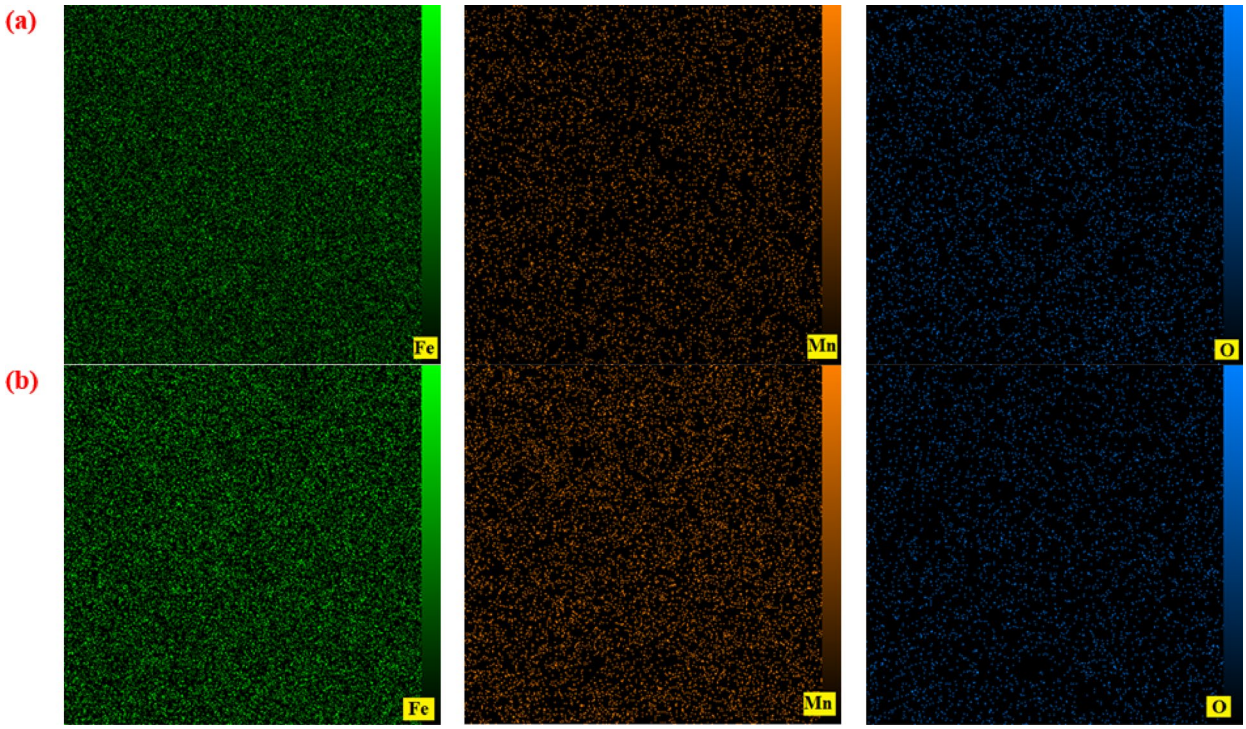


**Fig. 6**. Mapping images of electrodeposited 20Fe-80Mn at different potentials: (**a**) electrodeposited at −1 V and (**b**) electrodeposited at −2 V.

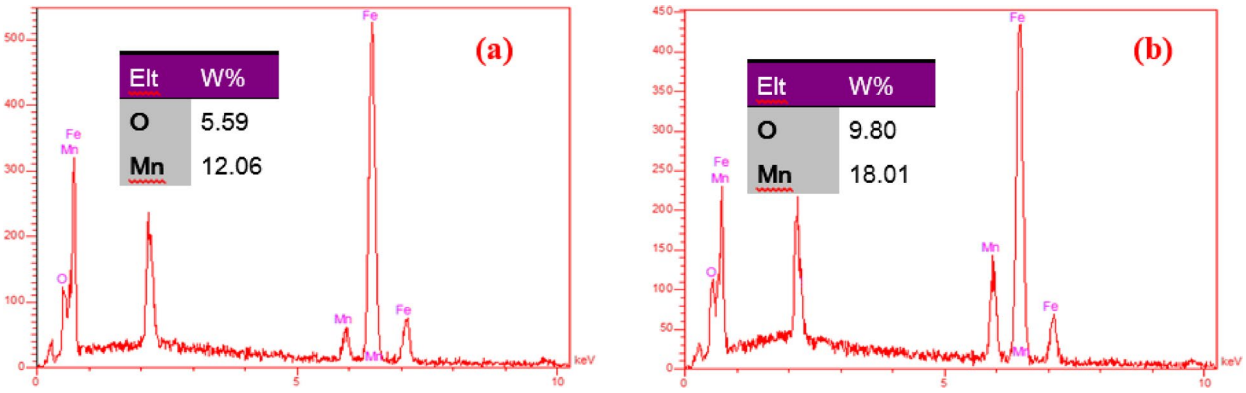


**Fig. 7**. EDX analysis of electrodeposited 20Fe-80Mn at different potentials: (**a**) electrodeposited at −1 V and (**b**) electrodeposited at −2 V.

80Mn-20Cu. Common to high-surface-area catalysts, its granular shape exposes more catalytic sites to the electrolyte by increasing the electrochemically active surface area. According to research on copper- and nickel-based catalysts, spherical grain shapes can enhance active site accessibility and promote gas release, both of which are advantageous for reaction kinetics[52–54]. The adsorption energy of oxygen intermediates (O*) in OER and hydrogen intermediates (H*) in HER is also probably decreased by the presence of Cu at the surface, which maximizes desorption and lowers overpotentials. Furthermore, the catalyst's higher performance is probably influenced by the particular elemental distribution in the 20Fe-80Mn-20Cu alloy. According to this composition, Fe and Cu are mostly present, with Mn playing a supporting function at a lower percentage. Every component contributes unique benefits to the catalytic processes: While Mn is present in lower concentrations, it can help with extra oxygen intermediate stability for OER, Cu optimizes hydrogen adsorption for HER and adds to charge transfer efficiency, and Fe improves oxygen evolution by stabilizing oxygen-containing intermediates. The alloy's structural stability may be further preserved by the lower Mn content, which also helps avoid problems with excessive oxophilicity that Mn may cause at greater concentrations and which could otherwise hinder HER[55]. Therefore, with Fe and Cu as the main components and Mn as a strategic additive, the optimal ratio seems to successfully balance both HER and OER activities, resulting in a catalyst surface that is perfect for water splitting.

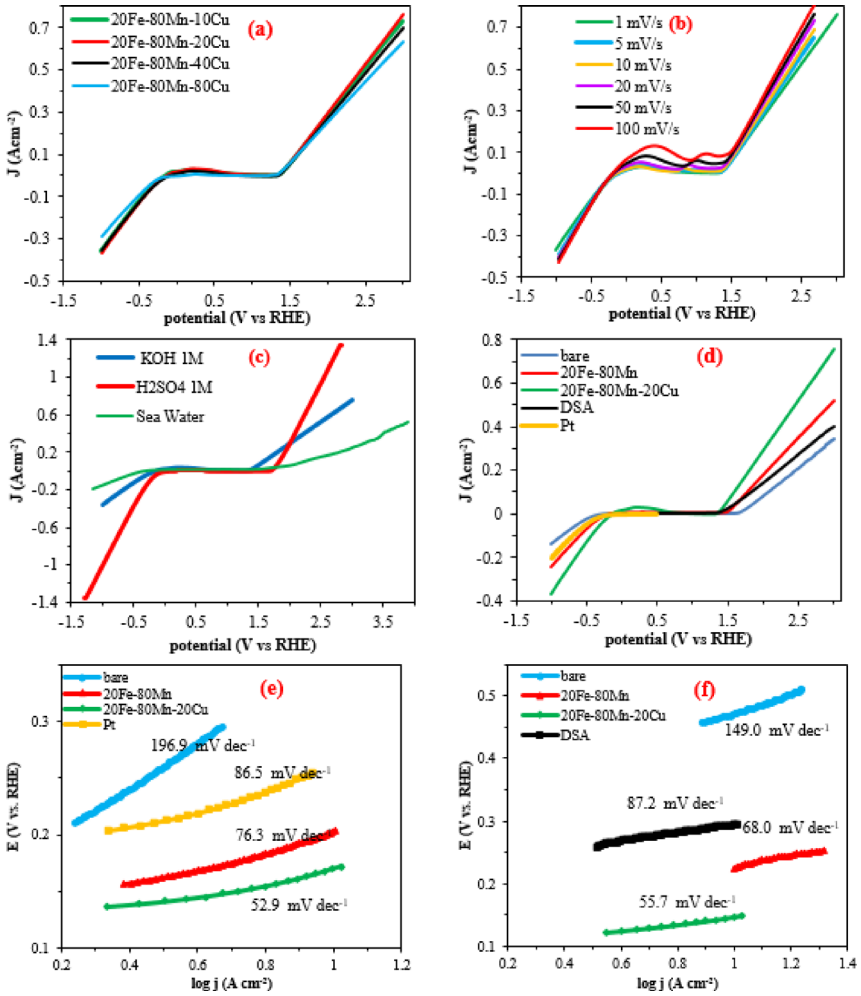


**Fig. 8**. (**a**) LSV diagrams of the electodeposited electrodes with different concentrations of Cu added to the electrodeposition bath 20Fe-80Mn electrode in KOH 1 M, (**b**) LSV diagrams of the electodeposited 20Fe-80Mn-20Cu electrode at different scan rate in KOH 1 M, (**c**) LSV diagrams of the electodeposited 20Fe-80Mn-20Cu electrode in different electrolytes, (**d**) LSV diagrams of different electrodes under study in KOH 1 M, (**e**) Tafel slopes of different electrodes– HER part in KOH 1 M, and (**f**) Tafel slopes of different electrodes– OER part in KOH 1 M.

The catalytic performance of the optimized ternary alloy 20Fe-80Mn-20Cu was compared to that of the binary alloy (20Fe-80Mn), the bare steel substrate, and benchmark electrodes—pure Pt for HER and dimensionally stable anode (DSA, with 30% Ir and 15% Ru) for OER. The 20Fe-80Mn-20Cu alloy achieved a performance that was comparable to or better than those of Pt and DSA in both HER and OER, as seen in Fig. 8d, considerably outperforming both the binary alloy and the bare substrate. This demonstrates the exceptional potential of this ternary alloy as an affordable substitute for catalysts made of noble metal.

The Tafel slopes (Fig. 8e and f) further elucidate the mechanistic pathways of HER and OER on these electrodes. For HER, the Tafel slope of 20Fe-80Mn-20Cu (53 mV $dec^{-1}$) was significantly lower than those of Pt (86 mV $dec^{-1}$), the binary alloy (76 mV $dec^{-1}$), and the steel substrate (197 mV $dec^{-1}$). We attribute this to synergistic effects: Fe and Mn stabilize the alloy matrix, while Cu optimizes hydrogen binding energy, thereby influencing intermediate coverage and the rate-determining step. For OER, the 20Fe-80Mn-20Cu alloy exhibited the lowest Tafel slope (56 mV $dec^{-1}$) compared to DSA (87 mV $dec^{-1}$), the binary alloy (68 mV $dec^{-1}$), and the steel substrate (149 mV $dec^{-1}$). The reduced slope implies a mechanistic advantage, likely due to the alloy's ability to stabilize oxygen-containing intermediates. Here, Cu promotes electron transfer, while Fe and Mn increase active-site availability and intermediate stabilization, collectively lowering the energetic barrier for oxygen evolution. For the HER, the Volmer-Heyrovsky mechanism dominates[56], where water dissociation ($H_2O + e^- \rightarrow H^* + OH^-$) occurs preferentially at Fe/Mn sites, followed by hydrogen recombination ($H^* + H_2O + e^- \rightarrow H_2 + OH^-$) facilitated by Cu's optimal H* adsorption properties - consistent with the observed 52.9 mV/dec Tafel slope (Fig. 8) and low charge-transfer resistance (Fig. 12a). For the OER, lattice oxygen participation occurs via sequential steps: (1) M-OH deprotonation to form M-O* (rate-limiting step at Mn/Fe sites, 56 mV/dec slope), (2) nucleophilic $OH^-$ attack on M-O* to form M-OOH (stabilized by Cu-induced charge redistribution), and (3) $O_2$ release - where post-test XRD (Fig. 3) shows $Cu_2O$ formation preserves the active interface. This dual functionality stems from

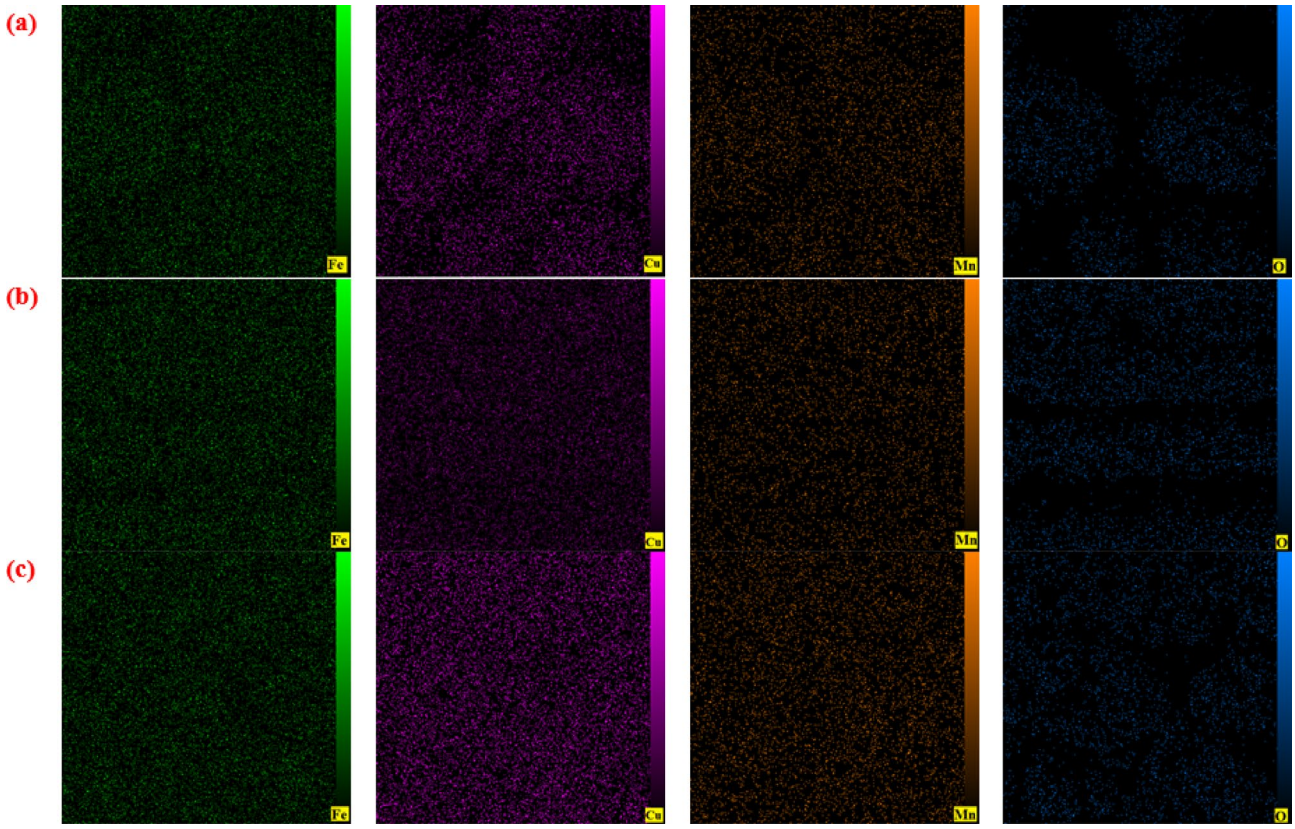


**Fig. 9**. Mapping images of electrodeposited 20Fe-80Mn-20Cu at −2 V (**a**) 20Fe-80Mn-20Cu electrode before stability test (**b**) 20Fe-80Mn-20Cu after stability (Chronopotentiometry at −250 mA for 4 day) (**c**) 20Fe-80Mn-20Cu after stability (Chronopotentiometry at + 250 mA for 4 day).

the ternary system's unique electronic structure, where Mn optimizes OER intermediates while Cu tunes HER energetics, as demonstrated in comparable systems.

## EIS and ECSA analyses

The EIS data (Figs. 13a and b) show the charge-transfer resistance and capacitive behavior of each electrode during HER and OER. The semicircle diameter in these Nyquist diagrams represents the charge-transfer resistance (Rct), which has a direct impact on the efficiency of catalysts. Smaller semicircle diameters show reduced charge-transfer resistance, which means that electrons may flow more easily between the electrode surface and the electrolyte's reactants, promoting catalytic processes.

The 20Fe-80Mn-20Cu alloy showed a much smaller semicircle diameter for HER (Fig. 13a) than both Pt and steel, indicating a lower $R_{ct}$ and more effective electron transfer. The semicircle diameter of 20Fe-80Mn-20Cu was slightly lower than that of 20Fe-80Mn, indicating the additional improvement in catalytic performance that Cu brought to the ternary alloy. The enhanced electronic conductivity and optimized active sites in 20Fe-80Mn-20Cu, where the inclusion of Cu probably enhances the adsorption and desorption of hydrogen intermediates, are responsible for the decrease in $R_{ct}$ for HER. The smaller Tafel slope for 20Fe-80Mn-20Cu in the HER LSV analysis is consistent with faster reaction kinetics created by this efficient electron transport. The potential of Fe-Mn-Cu systems to provide competitive HER performance at a fraction of the price of noble metals is highlighted by the lower semicircle diameter of these alloys when compared to Pt.

In the OER Nyquist diagrams (Fig. 13b), a similar trend is observed; however, the impact of Cu addition becomes even more pronounced. The 20Fe-80Mn-20Cu alloy composition showed a smaller semicircle diameter than both the 20Fe-80Mn alloy and the DSA, which is often used as a standard to assess the effectiveness of OER catalysis. The notable distinction between the semicircle diameters of the 20Fe-80Mn-20Cu alloy and the 20Fe-80Mn alloy, especially when compared to the properties of HER, suggests that Cu plays an even more crucial role in enhancing electron transfer mechanisms that are particularly important to OER. It is commonly known in the area that Cu can stabilize oxygen intermediates, which subsequently improves the efficiency of charge transfer while lowering the energy barrier linked to the OER route. These elements directly contribute to the further reduction in the charge transfer resistance for the OER, which indicates that the 20Fe-80Mn-20Cu alloy can more effectively support the reactions of oxygen intermediates, which will ultimately speed up the overall reaction kinetics[57].

Figure 13c and d presents the LSV curves of the studied catalysts, normalized by their respective ECSA values. Notably, the trends observed in the normalized LSV diagrams (Fig. 13c and d) remained consistent with

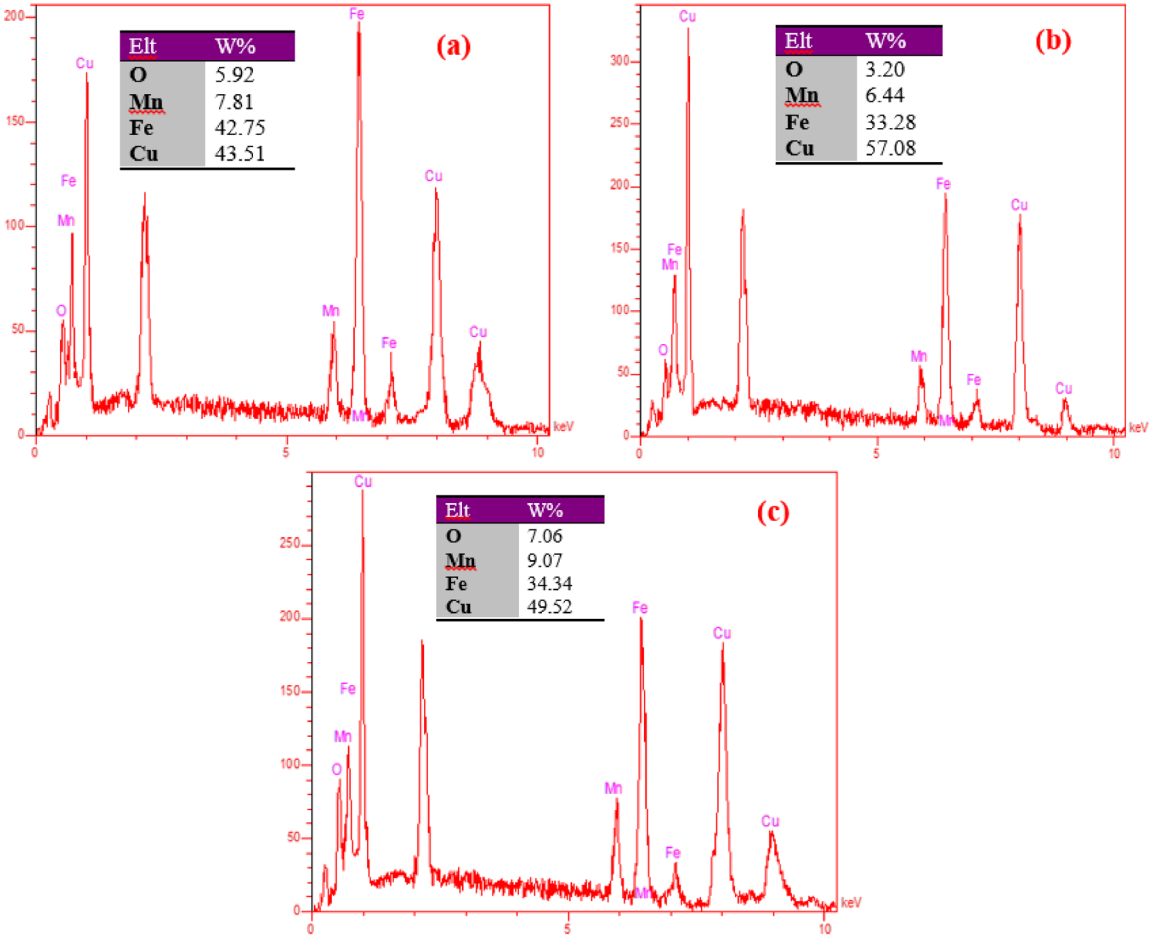


**Fig. 10**. EDX analysis of electrodeposited 20Fe-80Mn-20Cu at −2 V (**a**) 20Fe-80Mn-20Cu electrode before stability test (**b**) 20Fe-80Mn-20Cu after stability (Chronopotentiometry at −250 mA for 99 h) (**c**) 20Fe-80Mn-20Cu after stability (Chronopotentiometry at + 250 mA for 97 h).

those in the non-normalized data (Fig. 8d), confirming that the intrinsic catalytic activity—rather than surface area variations—governed the performance differences among the catalysts.

## Stability of catalysts

The chronopotentiometric stability evaluation of the 20Fe-80Mn-20Cu catalyst provided valuable insights into both its durability and energy efficiency under rigorous electrochemical circumstances for HER and OER. Figure 14 shows the chronopotentiometric curves at current densities of -250 mA $cm^{-2}$ for HER and + 250 mA $cm^{-2}$ for OER. Obviously, a considerable decrease in voltage requirements was achieved when using the 20Fe-80Mn-20Cu-coated electrode compared to the bare steel substrate. This voltage decrease of about 5 V for HER (from 8.1 V to 3 V) and 5.5 V for OER (from 8.8 V to 3.3 V) shows the catalyst's exceptional activity and efficiency, which are especially important for large-scale applications that require considerable energy savings. Given the impact of a 1 $cm^2$ electrode, scaling this system could lead to substantial energy reductions, making 20Fe-80Mn-20Cu an attractive option for commercial water-splitting.

The catalyst showed remarkable longevity over 4 days of continuous testing under these conditions, with just a little drop in performance—approximately 7% for HER and 5% for OER. These findings highlight the catalyst's robustness, which is essential for practical applications where extended use at high current densities can cause material deterioration and activity loss. The stability of each element under HER and OER conditions may be inferred from the SEM and EDX examinations of the catalyst surface before and after the stability tests, which show certain compositional and morphological changes (Figs. 9 and 10). After 4 days of HER electrolysis, SEM images showed a small peeling of the catalyst layer from the substrate (Fig. 11b), and OER showed comparable damage (Fig. 11c), albeit less severe. This little peeling may be a sign of a slight detachment of the material due to physical or electrochemical stresses imposed during prolonged catalytic activity. Such a phenomenon is commonly reported in the literature for materials subjected to high current densities in corrosive alkaline environments[59,60]. The EDX data also showed minor compositional changes, which are probably the result of element redistribution and/or dissolution during operation. Following 4 days of HER testing, Mn content decreased from 7.8 wt% to 6.4 wt%, Fe content reduced from 42.7 wt% to 33.3 wt%, and Cu content increased from 43.5 wt% to 57 wt%. This shift suggests that Mn and Fe are more prone to dissolution or surface rearrangement during HER, whereas Cu

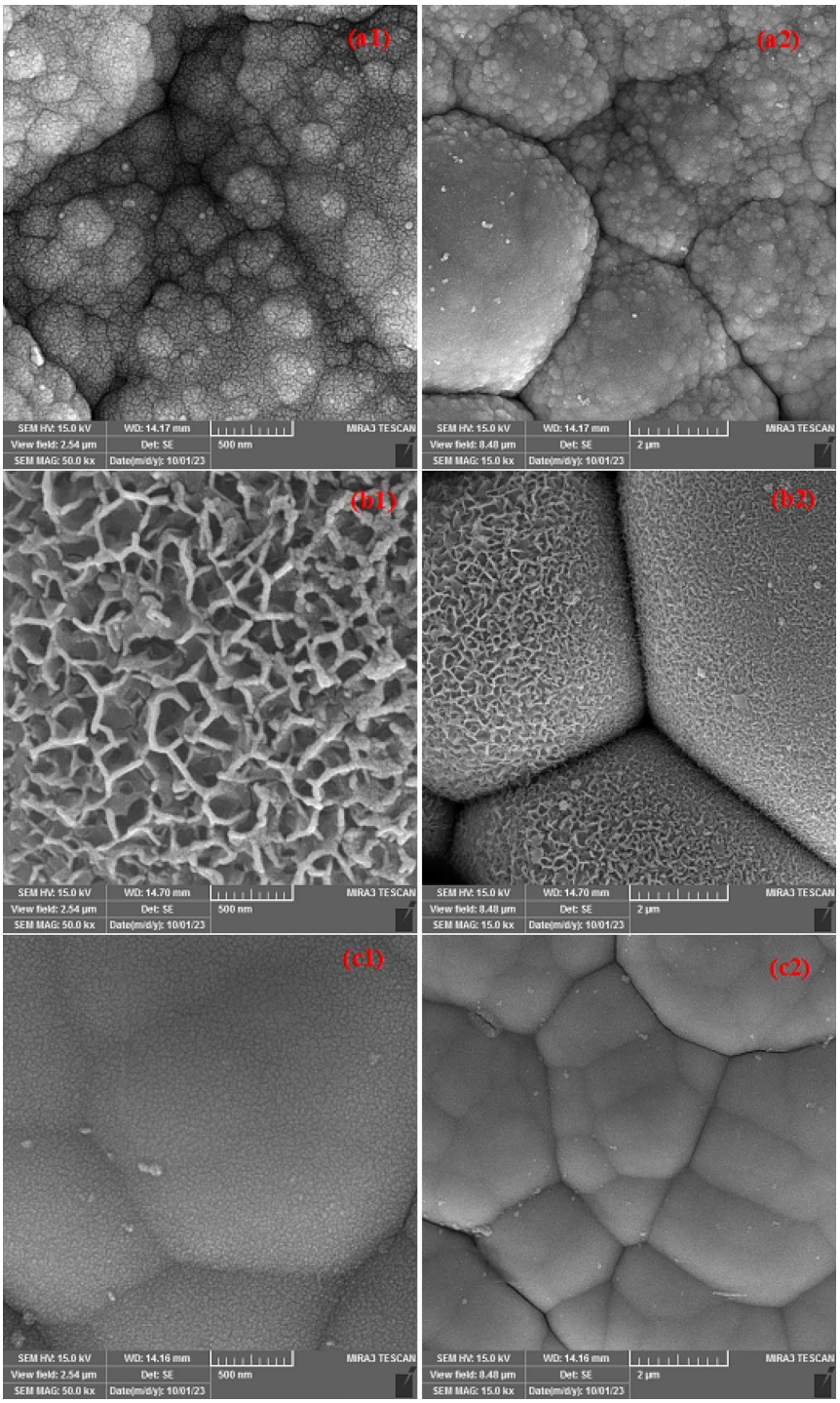


**Fig. 11**. FE-SEM images of electrodeposited 20Fe-80Mn-20Cu at −2 V (**a**) 20Fe-80Mn-20Cu electrode before stability test, (**b**) 20Fe-80Mn-20Cu after stability (Chronopotentiometry at −250 mA for 4 day), and (**c**) 20Fe-80Mn-20Cu after stability (Chronopotentiometry at + 250 mA for 4 day).

appears to remain relatively stable, with its increased surface presence potentially because of the dissolution or depletion of Fe and Mn. The slight reduction in oxygen content (from 5.9 wt% to 3.2 wt%) could indicate partial removal of surface oxide species under the high reducing conditions of HER. This is consistent with published research showing that surface oxygen and less stable alloy components tend to decrease with extended cathodic polarization[61,62]. For the OER stability, the EDX analysis post-testing indicates a similar trend, with Mn at 9 wt%, Fe at 34.3 wt%, and Cu at 49.5 wt%, implying that the high oxidative environment of OER likely leads to modest Fe dissolution, whereas Cu and Mn maintain a stronger presence. Oxygen content, however, increased to 7.1 wt%, showing that the anodic environment of OER promotes the formation or retention of oxides, which

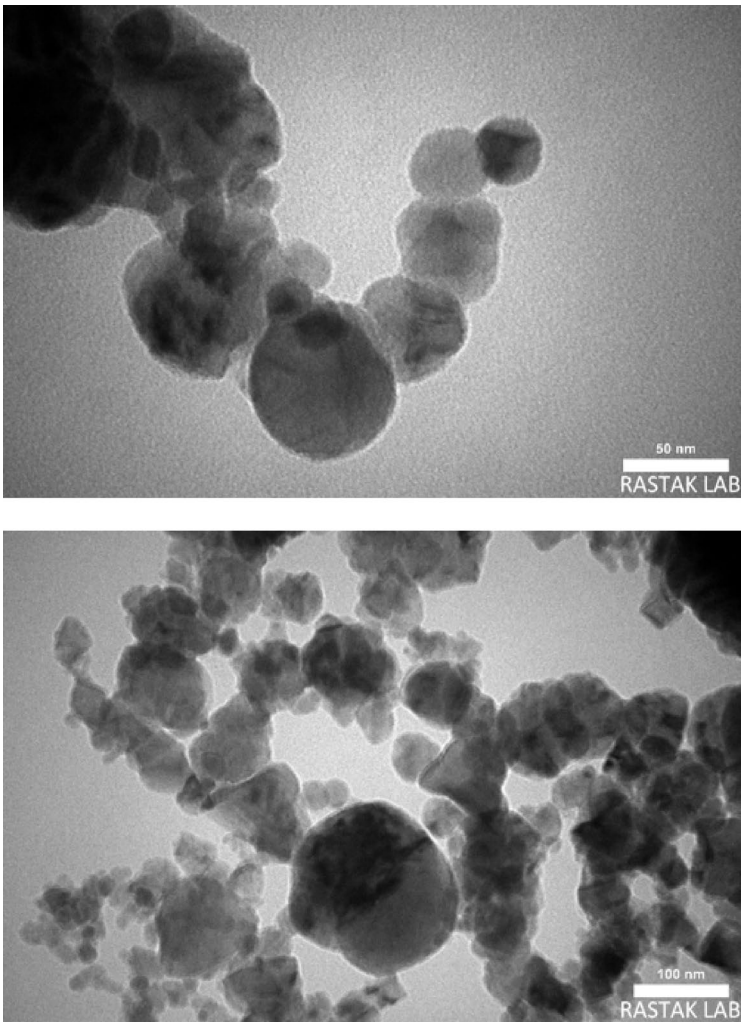


**Fig. 12**. TEM images of electrodeposited 20Fe-80Mn-20Cu.

have been shown to improve catalytic performance and stability in alkaline OER applications[63]. These findings were complemented by the XRD data provided for the 20Fe-80Mn-20Cu sample after HER and OER stability test. The post-HER spectrum remains nearly identical to the pre-reaction pattern, indicating excellent structural stability during hydrogen evolution. Accordingly, the XRD spectrum exhibited a peak at 39° and 43°, indexed to the (111) and (200) planes which is an indication of copper oxide formed on the catalyst[64]. These oxides, which have been well-documented for their better catalytic properties in OER, may contribute to the alloy's exceptional performance and stability in oxidative environments. Overall, it could be noted that the XRD spectra obtained from the catalyst following the rigorous stability test revealed no significant changes, confirming that the core crystalline structure remained fundamentally intact despite the observed compositional shifts. The ICP-OES results revealed that the concentrations of cations released from Electrode 20Fe-80Mn-20Cu Alloy after 24 h of chronopotentiometric testing at a current density of + 250 mA $cm^{-2}$ were negligible, indicating minimal leaching of metal species from the electrode into the solution. The measured concentrations of iron, manganese, and copper were 9.2, 7.6, and 5.5 ppm, respectively.

This remarkable stability of the crystalline configuration is consistent with various reports indicating that alloys characterized by a robust metal matrix and stable oxide formation exhibit proper structural integrity when subjected to extended periods of HER and OER conditions. Moreover, the preservation of the crystalline phase implies that, although certain surface components may undergo insignificant dissolution or redistribution, the underlying alloy matrix is steel durable, which potentially plays a significant role in enhancing the catalyst's overall resilience and performance during water splitting. The stability results support the possibility of employing the 20Fe-80Mn-20Cu alloy as a high-performance, long-lasting electrocatalyst for both HER and OER. The small morphological and compositional alterations observed point to a self-optimizing mechanism in which selective dissolution and enrichment of Cu—an element known to improve stability in alkaline conditions—may contribute to long-term catalytic activity. The findings suggest an alloy composition and surface morphology that improve catalytic performance while retaining durability, making this ternary alloy a viable choice for effective, long-term water-splitting applications.

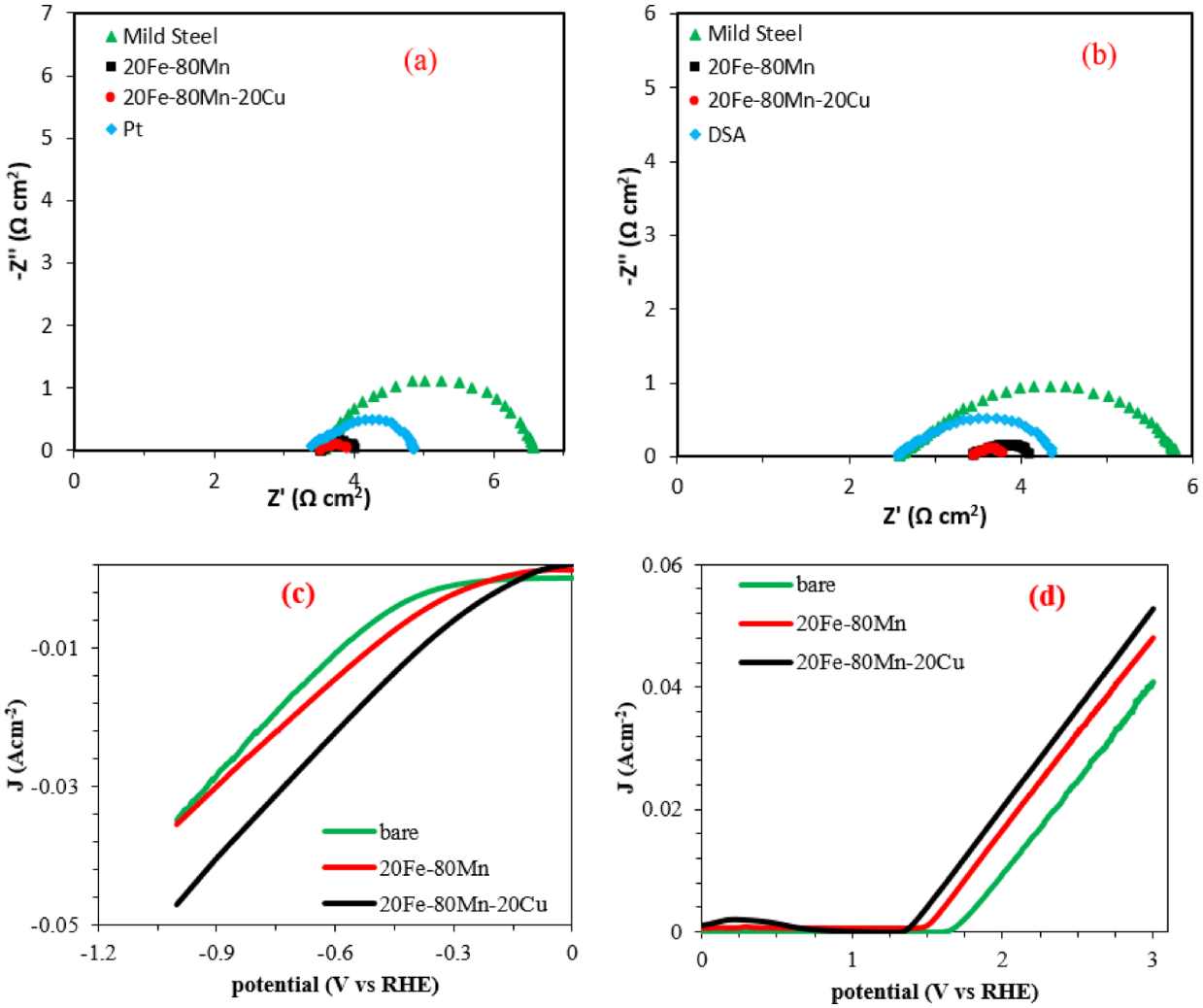


**Fig. 13**. EIS diagram of different electrodes in KOH 1M (**a**) HER part of electrodes at −1.2 V applied potential, (**b**) OER part of electrodes at + 2 V applied potential, (**a**) LSV diagrams Normalized by ECSA (HER part of electrodes), and (**d**) LSV diagrams Normalized by ECSA (OER part of electrodes).

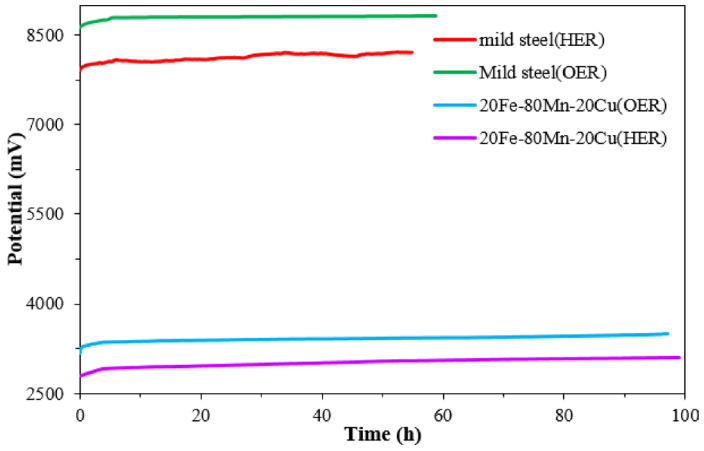


**Fig. 14**. Chronopotentiometry stability test of 20Fe-80Mn-20Cu and mild steel at + 250 mA for OER and − 250 for HER conditions.

| Electrode | Electrolyte | $\eta_{10}$ HER (mV) | $\eta_{10}$ OER (mV) | Tafel slope, HER (mV $dec^{-1}$) | Tafel slope, OER (mV $dec^{-1}$) | Stability (cycles/time) | Ref |
|---|---|---|---|---|---|---|---|
| $Pt_3Rh–Co_3O_4/C$ | 0.1 M $HClO_4$ | 55 | 290 | 38 | 63.4 | 5000 cycles (MA loss: 7–17%) | 65 |
| CFeCoNiP/NF | 1 M NaOH | 34 | 210 | 31 | 34 | 48 h @ 500 mA $cm^{-2}$ | 66 |
| Al-Ni-Co-Ir-Mo (HEA) | 0.5 M $H_2SO_4$ | 18 | 220 | 24 | 40 | 100 h @ 10 mA $cm^{-2}$ | 67 |
| hcp-NiFe@NC | 1 M KOH | N.D. | 226 | N.D. | 41 | 35 h @ 20 mA $cm^{-2}$ (7.2% loss) | 68 |
| NiFeMoCoCr HEA (FCC) | 0.5 M $H_2SO_4$ | 107 | N.D. | 41 | N.D. | 8 h @ 100 mA $cm^{-2}$ (no loss) | 65 |
| NiFeMoCoCr HEA (FCC) | 1 M KOH | 172 | N.D. | 66 | N.D. | Stable in alkaline/acidic | 65 |
| 20Fe-80Mn-20Cu | 1 M KOH | 172 | 147 | 52.9 | 55.7 | 4 days @ ±250 $mAcm^{-2}$ (no loss) | This work |

**Table 2**. Comparison electrocatalytic performance for HER and OER of catalyst of this work and those of literature.

This work introduces a novel transition-metal-based electrocatalyst that challenges the conventional limitations of bifunctional water-splitting catalysts. As evidenced by comparative performance data (see Table 2), our system achieves an optimal balance between hydrogen and oxygen evolution activity -a rare feat among both noble-metal and non-precious catalysts. Unlike previous approaches that typically sacrifice either stability or one half-reaction's efficiency, our design maintains competitive performance in both HER and OER while demonstrating exceptional durability under demanding operational conditions. The comparison with state-of-the-art systems in Table 1 reveals several key advantages: (1) comparable or superior activity to specialized HER or OER catalysts, but in a single bifunctional material; (2) significantly enhanced stability over extended operation compared to even noble-metal-containing systems; and (3) simpler composition than complex high-entropy alloys while maintaining similar catalytic profiles.

## Conclusions

This work suggests a thorough research of the electrocatalytic characteristics of Fe-Mn and Fe-Mn-Cu alloys for HER and OER in alkaline media. Following an initial optimization of binary Fe-Mn alloys, the 20Fe-80Mn composition was determined as the most active, with the lowest overpotentials for both HER and OER. The addition of Cu to the alloy improved catalytic activity even further, with the ternary 20Fe-80Mn-20Cu alloy surpassing both the binary alloy and benchmark electrodes such as Pt for HER and DSA for OER. EIS investigation revealed that 20Fe-80Mn-20Cu has a lower charge transfer resistance than both the binary alloy and reference electrodes, which is likely responsible for its higher catalytic efficiency. Stability tests showed that the 20Fe-80Mn-20Cu alloy was highly durable, with negligible activity loss over extended operating times in HER and OER, indicating its suitability for possible practical applications. Characterization data, such as SEM, Raman, IR, and XRD, demonstrated that the addition of Cu considerably affected the surface morphology, composition, and crystallographic characteristics, adding structural and chemical aspects useful for catalysis. This work provides insights into the rational design of cost-effective, high-performance ternary alloy catalysts, suggesting that Fe-Mn-Cu systems are promising candidates for sustainable water-splitting applications.

## Data availability

All data generated or analysed during this study are included in this published article [and its supplementary information files].

Received: 24 January 2025; Accepted: 14 May 2025
Published online: 19 May 2025

## References

1. Tee, S. Y. et al. Recent progress in energy-driven water splitting. *Adv. Sci.* **4**, 1600337 (2017).
2. Hosseini, S. E. & Wahid, M. A. Hydrogen production from renewable and sustainable energy resources: promising green energy carrier for clean development. *Renew. Sustain. Energy Rev.* **57**, 850–866 (2016).
3. Kaygusuz, K. Energy for sustainable development: A case of developing countries. *Renew. Sustain. Energy Rev.* **16**, 1116–1126 (2012).
4. Jamali, H. et al. Prolonged corrosion protection via application of 4-ferrocenylbutyl saturated carboxylate ester derivatives with superior Inhibition performance for mild steel. *Sci. Rep.* **14**, 13847 (2024).
5. Mugheri, A. Q. et al. Facile efficient Earth abundant NiO/C composite electrocatalyst for the oxygen evolution reaction. *RSC Adv.* **9**, 5701–5710 (2019).
6. Yue, M. et al. Hydrogen energy systems: A critical review of technologies, applications, trends and challenges. *Renew. Sustain. Energy Rev.* **146**, 111180 (2021).
7. Ishaq, H., Dincer, I. & Crawford, C. A review on hydrogen production and utilization: challenges and opportunities. *Int. J. Hydrog. Energy*. **47**, 26238–26264 (2022).
8. Mugheri, A. Q., Otho, A. A. & Mugheri, A. A. Hierarchical fibrous bimetallic electrocatalyst based on ZnO-MoS2 composite nanostructures as high performance for hydrogen evolution reaction. *J. Electroanal. Chem.* **883**, 115061 (2021).
9. Fajrina, N. & Tahir, M. A critical review in strategies to improve photocatalytic water splitting towards hydrogen production. *Int. J. Hydrog. Energy*. **44**, 540–577 (2019).
10. Mugheri, A. Q. et al. Efficient tri-metallic oxides NiCo 2 O 4/cuo for the oxygen evolution reaction. *RSC Adv.* **9**, 42387–42394 (2019).

11. Wang, X. et al. CoFeNiMnZnB as a high-entropy metal boride to boost the oxygen evolution reaction. *ACS Appl. Mater. Interfaces.* **14**, 48212–48219 (2022).
12. You, B. & Sun, Y. Innovative strategies for electrocatalytic water splitting. *Acc. Chem. Res.* **51**, 1571–1580 (2018).
13. Liu, Y. et al. Research progress of oxygen evolution reaction catalysts for electrochemical water splitting. *ChemSusChem* **14**, 5359–5383 (2021).
14. Mugheri, A. Q. et al. An advanced and efficient Co 3 O 4/C nanocomposite for the oxygen evolution reaction in alkaline media. *RSC Adv.* **9**, 34136–34143 (2019).
15. Moradi-Alavian, S. et al. Promotion of Hydrogen Evolution from Seawater via Poly (aniline-co-4-Nitroaniline) combined with 3D Nickel Nanoparticles. Sci. Rep. 13, 21486 (2023).
16. Peng, P. et al. Binary transition-metal oxide Hollow nanoparticles for oxygen evolution reaction. *ACS Appl. Mater. Interfaces*. **10**, 24715–24724 (2018).
17. Udayakumar, A., Dhandapani, P., Ramasamy, S., Yan, C. & Angaiah, S. Recent developments in noble metal–based hybrid electrocatalysts for overall water splitting. *Ionics (Kiel)*. **30**, 61–84 (2024).
18. Zhang, Y. et al. Next generation noble Metal-Engineered catalysts: from structure evolution to structure-Reactivity correlation in water splitting. *Adv. Funct. Mater.* **34**, 2308813 (2024).
19. Ashassi-Sorkhabi, H. et al. Electrodes Derived From Conducting Polymers and their Composites for Catalytic Conversion of Carbon Dioxide. J. Electrochem. Soc. 169, 124509 (2022).
20. Ahmed, I. et al. Design of industrially important Ir–W-Based electrocatalysts for alkaline bifunctional oxygen and hydrogen evolution reactions. *ACS Appl. Eng. Mater.* **2**, 2152–2163 (2024).
21. Wang, D. & Astruc, D. The recent development of efficient Earth-abundant transition-metal nanocatalysts. *Chem. Soc. Rev.* **46**, 816–854 (2017).
22. Ibn Shamsah, S. M. Earth-abundant electrocatalysts for water splitting: current and future directions. *Catalysts* **11**, 429 (2021).
23. Zheng, W., Li, Y. & Lee, L. Y. S. Earth-Abundant Metal-Based nanomaterials for electrochemical water splitting. *Funct. Nanomater. Synth. Prop. Appl.* 1–39 (2022).
24. Ha, J., Kim, M., Kim, Y. T. & Choi, J. Ni0. 67Fe0. 33 hydroxide incorporated with oxalate for highly efficient oxygen evolution reaction. *ACS Appl. Mater. Interfaces*. **13**, 42870–42879 (2021).
25. Dang, J. et al. Promoting the catalytic properties of the medium-entropy Co-Fe-Ni alloy toward water splitting and methanol oxidation by introducing a small amount of Cu and al. *J. Alloys Compd.* **1004**, 175935 (2024).
26. Wang, H. et al. The role of manganese-based catalyst in electrocatalytic water splitting: recent research and progress. *Mater. Today Phys.* 101169 (2023).
27. Huang, J. et al. Nano and phase engineering of Fe-Cu alloy exsolved perovskite oxide-based hetero-catalysts for efficient oxygen evolution reaction. *Fuel* **356**, 129479 (2024).
28. Han, T. et al. Study of OER electrocatalysts performance of Fe/Mn doped pyrochlorestructure. *J. Solid State Chem.* **303**, 122457 (2021).
29. Luo, J. et al. One-pot synthesis of Mn–Fe bimetallic oxide heterostructures as bifunctional electrodes for efficient overall water splitting. *Nanoscale* **12**, 19992–20001 (2020).
30. Liu, J. et al. The high-efficiency electrochemical catalysis of nitrogen-doped carbon nanotubes materials modified with Cu–Fe oxide alloy nanoparticles for HER and ORR. *Int. J. Hydrog. Energy*. **47**, 34090–34101 (2022).
31. Aksyanov, I. G., Kompan, M. E., Kul'kova, I. V. & Stepanov, Y. P. Luminescence and Raman spectra of sol-gel-derived ZnO microcrystals with a high iron content. *Glas Phys. Chem.* **38**, 143–148 (2012).
32. Li, J. et al. The role of iron oxide in the highly effective Fe-modified Co 3 O 4 catalyst for low-temperature CO oxidation. *RSC Adv.* **3**, 12409–12416 (2013).
33. Lin, Y. et al. Petal cell-derived MnO nanoparticle-incorporated biocarbon composite and its enhanced lithium storage performance. *J. Mater. Sci.* **55**, 2139–2154 (2020).
34. Mironova-Ulmane, N. et al. Synthesis and vibration spectroscopy of nano-sized manganese oxides. (2018).
35. Murthy, P. S. et al. IEEE,. Antibiofilm activity of nano sized CuO. in International conference on nanoscience, engineering and technology (ICONSET 2011) 580–583 (2011).
36. Rahimpour, E., Amini, M., Khandar, A. A. & Seidi, F. Azide–alkyne cycloaddition reactions over cobalt (0) nanoparticles supported on CaTiO3 perovskite. Sci. Rep. 15, 1–13 (2025).
37. Everbroeck, T., Van, Ciocarlan, R. G., Hoey, W., Van, Mertens, M. & Cool, P. Copper-containing mixed metal oxides (Al, Fe, Mn) for application in three-way catalysis. *Catalysts* **10**, 1344 (2020).
38. Du, H., Williams, C. T., Ebner, A. D. & Ritter, J. A. In situ FTIR spectroscopic analysis of carbonate transformations during adsorption and desorption of CO2 in K-Promoted HTlc. *Chem. Mater.* **22**, 3519–3526 (2010).
39. Jenkins, D. M. Empirical study of the infrared lattice vibrations (1100–350 cm – 1) of phlogopite. *Phys. Chem. Min.* **16**, 408–414 (1989).
40. Kumar, R., Kumar, S., Sahu, R. K. & Kailath, A. J. Atomic investigation of corrosion mechanism and surface degradation of Fe–Cr–Ni alloy in presence of water: advance reactive molecular dynamics simulation. *Trans. Indian Inst. Met.* **77**, 1355–1359 (2024).
41. Karar, N. & Jain, V. Correlating properties of alloys with constituent phases and their Raman spectra. *AIP Adv* **13**, (2023).
42. Betancourt-Galindo, R. et al. Synthesis of copper nanoparticles by thermal decomposition and their antimicrobial properties. *J. Nanomater.* 980545 (2014). (2014).
43. Hirano, Y., Kasai, Y., Sagata, K. & Kita, Y. Unique approach for transforming glucose to C3 platform chemicals using metallic iron and a Pd/C catalyst in water. *Bull. Chem. Soc. Jpn.* **89**, 1026–1033 (2016).
44. Langford, J., Il & Wilson, A. J. C. Scherrer after Sixty years: a survey and some new results in the determination of crystallite size. *J. Appl. Crystallogr.* **11**, 102–113 (1978).
45. Wróbel, J. S., Nguyen-Manh, D., Lavrentiev, M. Y., Muzyk, M. & Dudarev, S. L. Phase stability of ternary Fcc and Bcc Fe-Cr-Ni alloys. *Phys. Rev. B*. **91**, 24108 (2015).
46. Mourdikoudis, S., Pallares, R. M. & Thanh, N. T. K. Characterization techniques for nanoparticles: comparison and complementarity upon studying nanoparticle properties. *Nanoscale* **10**, 12871–12934 (2018).
47. Eissa, A. A. S., Kim, N. H. & Lee, J. H. Rational design of a highly mesoporous Fe–N–C/Fe 3 C/C–S–C nanohybrid with dense active sites for Superb electrocatalysis of oxygen reduction. *J. Mater. Chem. A*. **8**, 23436–23454 (2020).
48. Wang, H., Kang, X. & Han, B. Electrocatalysis in deep eutectic solvents: from fundamental properties to applications. *Chem. Sci.* (2024).
49. Zhang, T., Walsh, A. G., Yu, J. & Zhang, P. Single-atom alloy catalysts: structural analysis, electronic properties and catalytic activities. *Chem. Soc. Rev.* **50**, 569–588 (2021).
50. Li, Z., Wang, Y. & Lee, L. Y. S. Recent advances in synergistic modulation of Transition-metal-based electrocatalysts for water oxidation: a mini review. *Catalysts* **13**, 1230 (2023).
51. Zhang, W. et al. Fe-based dual-atom catalysts for oxygen reduction reaction. *J. Mater. Chem. A* (2023).
52. Kukushkin, R. G. & Yeletsky, P. M. Ni-Based Catalysts: Synthesis and Applications Today. *Catalysts* **13**, 968 (2023).
53. Finiels, A., Fajula, F. & Hulea, V. Nickel-based solid catalysts for ethylene oligomerization–a review. *Catal. Sci. Technol.* **4**, 2412–2426 (2014).
54. Shi, Y. F., Ma, S. & Liu, Z. P. Copper-based catalysts for CO 2 hydrogenation: a perspective on active sites. *EES Catal.* **1**, 921–933 (2023).

55. Kayode, G. O. & Montemore, M. M. Factors controlling oxophilicity and carbophilicity of transition metals and main group metals. *J. Mater. Chem. A*. **9**, 22325–22333 (2021).
56. Biswas, R. et al. Unraveling the role of orbital interaction in the electrochemical HER of the trimetallic AgAuCu nanobowl catalyst. *J. Phys. Chem. Lett.* **14**, 3146–3151 (2023).
57. Tahir, M. et al. Electrocatalytic oxygen evolution reaction for energy conversion and storage: A comprehensive review. *Nano Energy*. **37**, 136–157 (2017).
58. Ashassi-Sorkhabi, H., Kazempour, A., Moradi-Alavian, S., Asghari, E. & Lamb, J. J. 3D nanostructured nickel film supported to a conducting polymer as an electrocatalyst with exceptional properties for hydrogen evolution reaction. *Int. J. Hydrog. Energy*. **48**, 29865–29876 (2023).
59. Zhang, Z. et al. Bubbles management for enhanced catalytic water splitting performance. *Catalysts* **14**, 254 (2024).
60. Zang, B. et al. Design strategies of hydrogen evolution reaction nano electrocatalysts for high current density water splitting. *Nanomaterials* **14**, 1172 (2024).
61. Schöttner, L. et al. Structural evolution of α-Fe2O3 (0001) surfaces under reduction conditions monitored by infrared spectroscopy. *Front. Chem.* **7**, 451 (2019).
62. Favaro, M. et al. Elucidating the alkaline oxygen evolution reaction mechanism on platinum. *J. Mater. Chem. A*. **5**, 11634–11643 (2017).
63. Wang, J., Ren, Y. & Wang, P. Fe, F) co-doped nickel oxyhydroxide for highly efficient oxygen evolution reaction. *J. Mater. Chem. A*. **11**, 4619–4626 (2023).
64. Awad, M., Nawwar, M. & Zhitomirsky, I. Synergy of charge storage properties of CuO and polypyrrole in composite CuO-Polypyrrole electrodes for asymmetric supercapacitor devices. *ACS Appl. Energy Mater.* **7**, 5572–5581 (2024).
65. Zhang, G. et al. High entropy alloy as a highly active and stable electrocatalyst for hydrogen evolution reaction. *Electrochim. Acta*. **279**, 19–23 (2018).
66. Tsai, F. T. et al. The HER/OER mechanistic study of an FeCoNi-based electrocatalyst for alkaline water splitting. *J. Mater. Chem. A*. **8**, 9939–9950 (2020).
67. Jin, Z. et al. Nanoporous Al-Ni-Co-Ir-Mo high-entropy alloy for record-high water splitting activity in acidic environments. *Small* **15**, 1904180 (2019).
68. Wang, C., Yang, H., Zhang, Y. & Wang, Q. NiFe alloy nanoparticle with hexagonal close-packed crystal structure stimulates superior oxygen evolution reaction electrocatalytic activity. *Angew .Chem. Int. Ed.* **58**, 6099–6103 (2019).


## Acknowledgements

This work is supported by a research grant of the University of Tabriz (Grant No. 2024.03.09/3772).

## Author contributions

Saleh Moradi-Alavian: Investigation, Writing – Original, Draft Formal analysis Amir Kazempour: Investigation, Writing – Original, Draft Formal analysis Habib Ashassi-Sorkhabi: Validation, Editing, Elnaz Asghari: Supervision, Validation, Writing - Review & Editing.

## Declarations

## Competing interests

The authors declare no competing interests.

## Additional information

**Correspondence** and requests for materials should be addressed to E.A.

**Reprints and permissions information** is available at www.nature.com/reprints.

**Publisher's note** Springer Nature remains neutral with regard to jurisdictional claims in published maps and institutional affiliations.

**Open Access** This article is licensed under a Creative Commons Attribution-NonCommercial-NoDerivatives 4.0 International License, which permits any non-commercial use, sharing, distribution and reproduction in any medium or format, as long as you give appropriate credit to the original author(s) and the source, provide a link to the Creative Commons licence, and indicate if you modified the licensed material. You do not have permission under this licence to share adapted material derived from this article or parts of it. The images or other third party material in this article are included in the article's Creative Commons licence, unless indicated otherwise in a credit line to the material. If material is not included in the article's Creative Commons licence and your intended use is not permitted by statutory regulation or exceeds the permitted use, you will need to obtain permission directly from the copyright holder. To view a copy of this licence, visit http://creativecommons.org/licenses/by-nc-nd/4.0/.

© The Author(s) 2025